HAL
open science

Microstructural characterization of creep anisotropy at 673K in the M5® alloy

Martin Rautenberg, Xavier Feaugas, Dominique Poquillon, Jean-Marc Cloué

To cite this version:

Martin Rautenberg, Xavier Feaugas, Dominique Poquillon, Jean-Marc Cloué. Microstructural characterization of creep anisotropy at 673K in the M5® alloy. Acta Materialia, 2012, vol. 60, pp. 4319-4327. 10.1016/j.actamat.2012.04.001 . hal-00825276v1

HAL Id: hal-00825276

https://hal.science/hal-00825276v1

Submitted on 23 May 2013 (v1), last revised 28 May 2013 (v2)

HAL is a multi-disciplinary open access archive for the deposit and dissemination of scientific research documents, whether they are published or not. The documents may come from teaching and research institutions in France or abroad, or from public or private research centers.

L'archive ouverte pluridisciplinaire **HAL**, est destinée au dépôt et à la diffusion de documents scientifiques de niveau recherche, publiés ou non, émanant des établissements d'enseignement et de recherche français ou étrangers, des laboratoires publics ou privés.

Open Archive Toulouse Archive Ouverte (OATAO)
OATAO is an open access repository that collects the work of Toulouse researchers and makes it freely available over the web where possible.

This is an author-deposited version published in: http://oatao.univ-toulouse.fr/
Eprints ID: 8718

To link to this article : DOI:10.1016/j.actamat.2012.04.001
URL : http://dx.doi.org/10.1016/j.actamat.2012.04.001

To cite this version:
Rautenberg, Martin and Feaugas, Xavier and Poquillon, Dominique and Cloué, Jean-Marc *Microstructural characterization of creep anisotropy at 673K in the M5® alloy*. (2012) Acta Materialia, vol. 60 (n° 10). pp. 4319-4327. ISSN 1359-6454

Any correspondence concerning this service should be sent to the repository administrator: staff-oatao@listes.diff.inp-toulouse.fr

Microstructural characterization of creep anisotropy at 673 K in the M5® alloy

Martin Rautenberg [a,b,*], Xavier Feaugas [c], Dominique Poquillon [b], Jean-Marc Cloué [a]

[a] AREVA, 10, rue Juliette Récamier, 69456 Lyon Cedex 06, France
[b] CIRIMAT, CNRS/UPS/INPT, 4 allée Emile Monso, 31030 Toulouse, France
[c] LEMMA, Université de La Rochelle, avenue Michel Crépeau, 17042 La Rochelle, France

Abstract

Zirconium alloy tubing is used in pressurized water nuclear reactors in order to prevent fissile material from leaking into the coolant. It can be the first safety wall of nuclear fuel, and is submitted to complex thermomechanical loadings. In consequence, new Nb-modified alloys, such as the M5® alloy, and fine numerical models are being developed to guarantee a better and longer mechanical integrity of these tubes. To identify the physical mechanisms that could be considered in such models, an experimental approach, combining creep tests with electron backscattered diffraction and Transmission electron microscopy investigations, was carried out.

Tubular specimens were submitted to multiaxial creep tests at a temperature of 673 K. Seven ratios between the axial and hoop applied stresses were investigated. It enabled a macroscopic evidence of the creep anisotropy. Besides, EBSD analyses on a mesoscopic-sized non deformed area led to the characterization of the variation of the average Schmid factor with the direction of loading. Finally, TEM observations were done on seven crept samples, corresponding to the seven directions of loading tested mechanically. The variations of the different parameters investigated (activated slip systems, dislocation densities, curvatures of the dislocations) can be seen as the effects of the creep anisotropy at a microscopic scale. The correlation between results is then discussed in a multiscale frame.
© 2012 Acta Materialia Inc. Published by Elsevier Ltd. All rights reserved.

Keywords: Zirconium (Zr); Creep; Anisotropy; Transmission electron microscope (TEM); Dislocation

1. Introduction

Zirconium alloys are widely used in the nuclear industry as a major core component in boiling water and pressurized water reactors. The thermal creep strength of these components is of prime importance to ensure the mechanical integrity of core structures during and after their use in the reactor. In consequence, thermal creep mechanisms have been widely studied during the past 50 years [1–5]. Although there is no consensus concerning the physical mechanisms involved, creep anisotropy of zirconium alloy tubing is generally accepted [6–11]. A better understanding of this phenomenon would lead to improvements in modeling and predictions of the creep behavior of core structures.

Creep anisotropy at 673 K for low strain levels is mainly due to a combination of two metallurgical properties. Firstly, the fabrication process of the tubes is at the origin of a strongly heterogeneous crystallographic texture [6,9]. Secondly, the limited number of possible slip systems and their orientation in the hexagonal close packed (hcp) lattice induce a localization of dislocation glide. Indeed, ab initio simulations [12,13] confirm that prismatic glide is more liable to occur than basal glide for alpha zirconium (αZr). These arguments may therefore explain a variation in the ease of dislocation glide with loading direction, which can be linked to the macroscopic anisotropy observed during tensile strengthening [10]. However, the consequences for

* Corresponding author at: CIRIMAT, CNRS/UPS/INPT, 4 allée Emile Monso, 31030 Toulouse, France. Tel.: +33 5 34 32 34 49; fax: +33 5 34 32 34 98.
E-mail address: mrautenb@gmail.com (M. Rautenberg).

http://dx.doi.org/10.1016/j.actamat.2012.04.001

creep behavior remain unclear. Moreover, developments of analytical descriptions of creep data, through computation using stress exponents [4] or Transmission electron microscopy (TEM) observations [5], suggest that dislocation climb could replace dislocation glide as a rate-controlling process at intermediate temperatures (673–1123 K). Thus, characterization of creep anisotropy needs new experimental data obtained at different length scales.

In the present work, we propose to investigate creep mechanisms on the M5® alloy at 673 K, using a multiscale approach to the effects of the loading direction. Thus, after a presentation of materials and characterization techniques, we will first focus on creep tests, which constitute a macroscopic characterization of creep anisotropy. Then, electron backscattered diffraction (EBSD) analyses, i.e. a mesoscopic scale characterization, are presented with an emphasis on the effect of crystallographic texture, presented through Schmid factor computations. These results led us to assume that strain could be carried mainly by prismatic and pyramidal dislocation glides along the $\langle a \rangle$ axis of the hcp lattice. Finally, this hypothesis is checked at a microscopic scale using TEM. At least 50 grains were observed on several specimens crept at 673 K under different multiaxial loadings (seven directions in stress space). This enabled a statistical quantification of the observed parameters: dislocation densities, activated slip systems, and curvature of dislocations. The evolution of these parameters with the direction of loading is discussed with regard to the creep test results and EBSD analysis. Our results suggest that cross-slip activation and long-range internal stresses can explain the anisotropy of creep in relation to the crystallographic texture.

2. Experimental features

2.1. Material

The M5® tubes used for this study were provided by AREVA. They were formed by a cold pilgering rolling process and then subjected to a final recrystallization heat treatment. These processes induce a fully recrystallized hcp alloy microstructure, with a strongly anisotropic crystallographic texture (Fig. 1). Grain sizes vary between 3 and 5 μm, and the zirconium content of the studied material is higher than 98.5%. The chemical composition of the M5® [14] is given in Table 1. Several second phase particles, due to alloying elements, are present in an α-matrix. To check those data, and to question the effects of the sample preparation process on the microstructure, we observed by TEM a thin foil taken on a non-deformed sample. No dislocations were observed inside the material before creep tests.

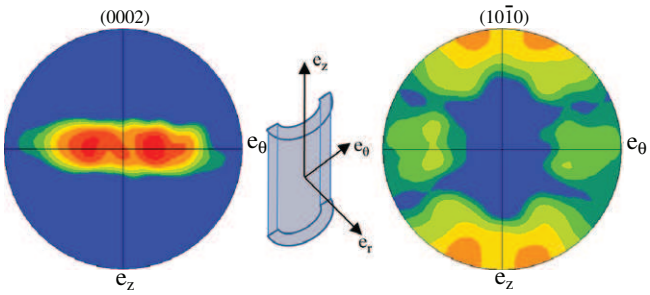

Fig. 1. (0002) and {10−10} pole figures of the recrystallized zirconium alloy (EBSD analysis performed on 20,000 grains).

Table 1
Chemical composition (in weight) of the M5®.

Nb (%)	O (ppm)	Fe (ppm)	Cr (ppm)	Zr
1	1450	370	41	Bal.

2.2. Mechanical tests

The specimens used for creep tests are 130 mm long, 0.5 mm thick cylinders cut from M5® tubes. The dimensional measurements and temperature regulation were made on a gauge of 20 mm long, centered on the middle of the specimens. Specimens are sealed by a clamping set before being subjected to creep tests with a specific device [15]. A constant temperature of 673 ± 2 K is maintained on the gauge using a radiative furnace. An axial load up to 5 kN can be applied simultaneously with an internal pressure up to 280 bars. As the specimens are thin-walled tubes, the radial stress can be ignored. We define the biaxial stress ratio $\beta = \sigma_{zz}/\sigma_{\theta\theta}$, with $\sigma_{\theta\theta}$ and σ_{zz} being respectively the applied axial and hoop stresses. The angle of the total applied stress with the axial direction is called α and we can set $\alpha = \arctan(1/\beta)$. Creep tests were stopped when stationary creep strain rate stabilized, leading to final equivalent creep strains between 1% and 3%.

2.3. Transmission electron microscopy method

Thin foils were cut parallel to the outer surface of the tested specimens, in the zone of the gauge. Thin foils were first mechanically ground to a thickness of 150 μm. They were then electrolytically polished with a Struers Tenu-Pol®, at a voltage of 15 V and a temperature of 243 K in a 10% perchloric acid–20% 2-butoxyethanol–70% methanol solution. In order to relate the crystallographic orientations to the loading directions, a notch corresponding to the axial direction was placed on each thin foil and orientated parallel to the tilt axis of the sample holder. The observations were carried out at a temperature of 293 K in a Jeol 2011 Transmission electron microscope working at 200 kV (tilt $\pm 25°$). For each of the seven directions explored under mechanical testing defined by α or β, at least 50 grains were randomly selected and observed under several diffraction conditions, to enable an accurate identification of their crystallographic orientations. Several electron diffraction patterns of each grain were used to build stereographic projections using the CaRIne Crystallography software [16]. The positions in a $\{e_\theta; e_z\}$ system of basal planes determined with this method (Fig. 2) are in

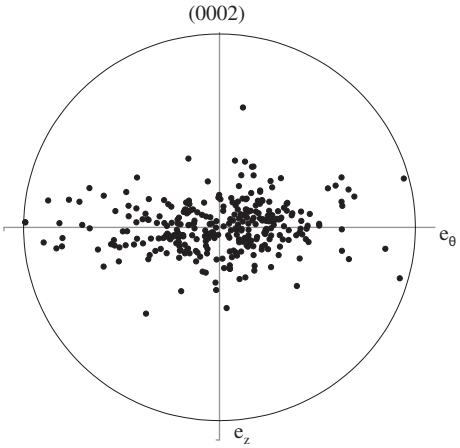

Fig. 2. (0002) Pole figures of the studied material (electron diffraction patterns analysis of the 350 grains observed by TEM).

good agreement with EBSD results (Fig. 1). This suggests that the population of observed grains is representative of the material microstructure.

TEM image analysis was carried out to determine the active slip systems, dislocation densities and their average radius of dislocation curvature. The latter was observed under different tilt conditions and is used to identify the habit plane of dislocation line and the long-range internal stresses acting on the dislocation line. Dislocation density was determined using the classical intersect method [17,18].

A slip system was considered to be active inside a grain when three or more distinct dislocation lines of this system could be observed. Therefore, any grain containing less than three dislocation lines for each of its potential slip systems was assumed to carry no plastic deformation. This semi-statistical approach has previously demonstrated its interest in different strengthening materials such as titanium alloys [19–21], zirconium alloys [22], austenitic stainless steel [23] and nickel [18,24].

2.4. Electron backscattered diffraction scanning

A sample was cut parallel to the outer surface of an as-received tube. The electropolishing was shorter than the one used for TEM specimens, to avoid a curving of the observation zone. The surface morphology was observed by scanning electron microscopy (SEM) with a FEI Quanta 200 ESEM-FEG operating at 25 kV. No significant roughness was noticed. EBSD was used to obtain the size, boundaries and orientations of grains on a $140 \times 75\ \mu m^2$ area. This surface corresponds to ~2000 grains. EBSD maps were acquired at the same acceleration voltage with the TSL OIM Data collection 5 software [25], using a step size of 400 nm. Grain size and orientation maps were then calculated using the TSL OIM Analysis 5 software [26]. In contrast to recent publications on titanium alloys [27] a correlation between slip lines associated with dislocation emergence and EBSD mapping cannot be used in the present work to identify slip systems. The crystallographic texture imposed in most cases that the Burgers vector $\langle a \rangle$ associated with the predominant slip (prismatic slip) is included in the $\{e_\theta; e_z\}$ plane. Moreover, the strain levels investigated here may be too low to enable an efficient detection of dislocation emergence by SEM observations. Nevertheless, geometric analysis of the possible activated slip systems can be proposed using EBSD data collected for each β or α situation studied.

3. Creep tests results

Recently, a critical analysis of the influence of complex loading paths was made to point out their effects on strain [10,11,22] and strain rate [15]. It was shown that, in comparison with uniaxial tests, zirconium alloys can exhibit either overstrengthening or oversoftening under multiaxial loading paths. To provide a comparison between the different stress paths in $(\sigma_{\theta\theta}, \sigma_{zz})$ space a specific testing method has been followed. The axial and hoop stresses can be combined in an equivalent stress using a von Mises criterion:

$$\sigma = \sigma_{VM} = \sqrt{1/2\left(\sigma_{\theta\theta}^2 + \sigma_{zz}^2 + (\sigma_{\theta\theta} - \sigma_{zz})^2\right)} \quad (1)$$

For each loading path, the measured stationary axial and hoop creep strain rates $\dot{\varepsilon}_{\theta\theta}$ and $\dot{\varepsilon}_{zz}$ can be used to calculate a von Mises equivalent strain rate in stage II creep:

$$\dot{\varepsilon} = \dot{\varepsilon}_{VM} = \sqrt{4/3\left(\dot{\varepsilon}_{\theta\theta}^2 + \dot{\varepsilon}_{zz}^2 + \dot{\varepsilon}_{\theta\theta}\dot{\varepsilon}_{zz}\right)} \quad (2)$$

A constant von Mises yield stress criterion is plotted on Fig. 3 for a value of $\sigma_{VM} = 7/6 \times \sigma_0$, σ_0 being the applied axial stress needed to give a measured strain rate of $3.5 \times 10^{-8}\ s^{-1}$, with the hoop stress set to zero. The factor 7/6 corresponds to the best description of experimental data with an isotropic criterion (Fig. 3b). For isotropic behavior, an applied stress of $7/6 \times \sigma_0$ would give this strain rate for any value of α.

An isocreep curve, i.e. the locus $[\sigma_{\theta\theta}; \sigma_{zz}]$ for a constant strain rate, can then be interpolated between experimental points using the Norton law:

$$\dot{\varepsilon} = A\sigma^n \quad (3)$$

where A and n are constants having different values for each α [15]. A comparison of the isocreep curve with the von Mises yield locus for $0° < \alpha < 90°$ leads to an illustration of the macroscopic creep anisotropy (Fig. 3b). Thus, using a von Mises criterion with $\sigma_{VM} = 7/6 \times \sigma_0$, the macroscopic behavior of the material can be defined as an "oversoftening" if α is out of the $[30°; 60°]$ angular range (domains A and C). The isotropic case would correspond here to higher creep stress loadings for the same strain rate. In contrast, an "overstrengthening" behavior can be related if α lies inside this interval (domain B). A comparison of the coordinates $[\sigma_{\theta\theta}/\sigma_0; \sigma_{zz}/\sigma_0]$ of crept specimens observed by TEM with the experimental isocreep curve at a strain rate of $3.5 \times 10^{-8}\ s^{-1}$, illustrates that each of them exhibits a quite similar equivalent strain rate. Thus this

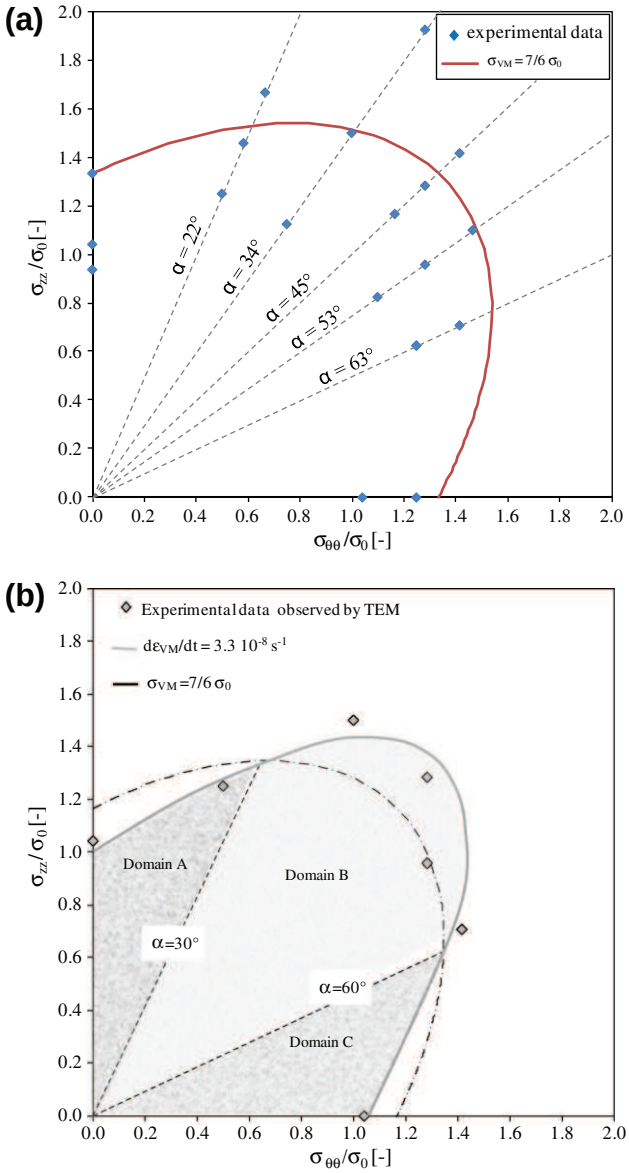

Fig. 3. (a) Applied stresses for the creep tests compared with a constant von Mises yield stress criterion; (b) isocreep curve obtained from the experimental data presented with the tests analyzed by TEM.

database can be used to probe the physical origin of the creep anisotropy.

In a first step, to bring a link between creep tests results and physical mechanisms at a microscopic scale, an apparent activation volume can be computed for each α angle. This parameter is defined as the macroscopic sensitivity of viscoplastic flow to the stress. If we consider thin-walled tubes, the apparent activation volume can be estimated with the following expression:

$$V_{\text{app}} = k_B T \frac{\partial \ln \dot{\varepsilon}}{\partial \sigma} \tag{4}$$

where $T = 673$ K is the temperature and k_B is the Boltzmann constant. We can do here a parallel between the apparent activation volume and the activation volume $V = M \cdot V_{\text{app}}$ locally depending on dislocation mobility, M

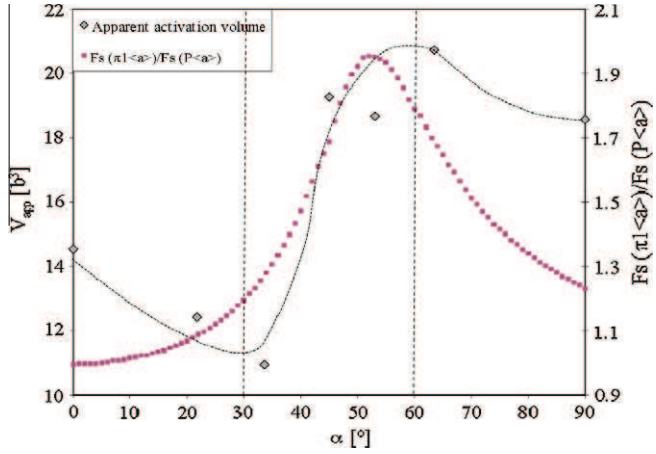

Fig. 4. Variation of the apparent activation volume (left axis) and the Schmid factors ratio (right axis) with the loading direction α.

being the Taylor factor [28]. The activation volume V corresponding to a particular deformation mechanism is related to the area swept by a dislocation between two stable positions. This area is multiplied by the Burgers vector length b to present the result as a volume, commonly expressed in b^3.

The value of V_{app} for each investigated loading direction is plotted in Fig. 4. Three domains can be distinguished on this plot. For $\alpha \leqslant 30°$ (domain A) we observe a decrease of V_{app}/b^3 between 14 and 11 with the increase of α.

In correlation with overstrengthening related to domain B, the increase of α results on a jump of V_{app}/b^3 to reach a value of 21. Finally, V_{app} stays quite constant in domain C. Neglecting the variation of the Taylor factor M for angular range associated with domain B, we can therefore assume that the increase of V_{app} can result from an evolution of the deformation mechanisms inside the grains. This result is valid on the strain rate range used to compute the activation volumes, i.e. $1 \times 10^{-9}\ \text{s}^{-1} < \dot{\varepsilon} < 2 \times 10^{-7}\ \text{s}^{-1}$. The mechanical behavior can be discussed with TEM and EBSD statistical data.

4. TEM and EBSD observations

Slip anisotropy is important in hcp structures [19,22,27–29] and, as a consequence, significant "microscopic" differences can exist between grains, depending on their crystallographic orientations with respect to the stress–strain axis. Thus the activation of slip systems can be a function of α. In order to explore this aspect, a statistical analysis has been made in term of geometric considerations using EBSD maps and in term of physical mechanisms using TEM observations.

4.1. Geometric consideration of slip activity: Schmid factors

In the case of thin-walled tubes under axial and hoop loadings, the Schmid factor F_{Si} of a slip system (i) can be written as [30]:

$$F_{\mathrm{Si}} = \frac{\sigma_{zz}\cos(\gamma_{zi})\cos(\varphi_{zi}) + \sigma_{\theta\theta}\cos(\gamma_{\theta i})\cos(\varphi_{\theta i})}{\max(\sigma_{zz};\sigma_{\theta\theta})} \quad (5)$$

where γ_{zi} and $\gamma_{\theta i}$ are the angles between the Burgers vectors and the axial or hoop direction, while φ_{zi} and $\varphi_{\theta i}$ are the angles between the normal vector of the slip plane and the axial or hoop direction. This expression was used to compute Schmid factors for different loading paths: $0° < \alpha < 90°$. We considered only dislocations with $\langle a\rangle$ Burgers vectors gliding inside prismatic planes (three $P\langle a\rangle$ slip systems per grain) or first order pyramidal planes (six $\pi_1\langle a\rangle$ slip systems). With a constant value of α, for each type of slip system ($P\langle a\rangle$ or $\pi_1\langle a\rangle$), the highest Schmid factors of every scanned grain were used to compute two average Schmid factors presented in Fig. 5. The variation of the average Schmid factor with the loading direction depends on the considered slip system. We find that dislocation glide for both types of slip systems gets more and more difficult for $0° < \alpha < 53°$, as F_S decreases with the increase of α. Then F_S increases until $\alpha = 90°$, without reaching the maximum values (obtained for an axial loading, at $\alpha = 0°$). Furthermore, the ratio between both average Schmid factors $F_S(Py1\langle a\rangle)/F_S(P\langle a\rangle)$ is at its maximum in the angular range which corresponds to domain B. Thus, from geometric considerations, the probability of $\pi_1\langle a\rangle$ dislocation glide in this interval (domain B) is higher than in the other domains (A and C).

These considerations need to be confirmed by direct observations of the activity of both slip systems using TEM investigations. Additionally, it has been reported in the past that prismatic slip is the easier slip system in term of critical resolved shear stresses.

4.2. Post-mortem TEM investigations of dislocation glide

From a qualitative point of view, the microstructures of the seven crept samples observed are the same although they underwent different loading directions (Fig. 3b). Furthermore, neither grain rotation nor twinning was observed. Dislocation lines are distributed homogeneously. After observing them under different tilts, their slip plane can be identified using a stereological method. Two kinds of dislocation line configurations can be observed: long straight dislocation lines (Fig. 6a) or dislocations with a large curvature (Fig. 6b) which are pinned at obstacles. In both cases, the local curvature offers the opportunity to identify the crystallographic plane containing the dislocation line, which is assimilated to the slip plane in the present work. As no dislocation line is partially or totally lying out of a slip plane,

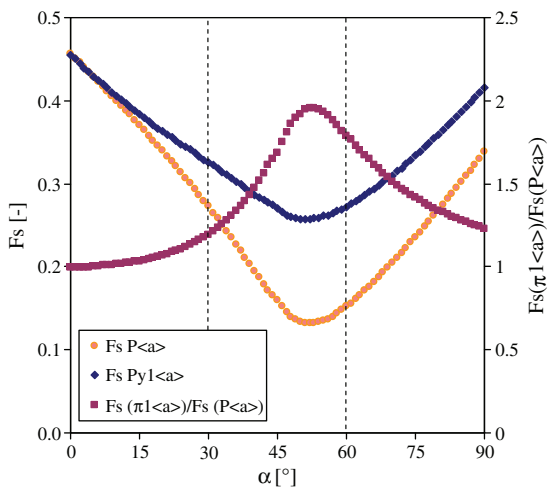

Fig. 5. Variation of average Schmid factors with the loading direction, calculated from EBSD maps.

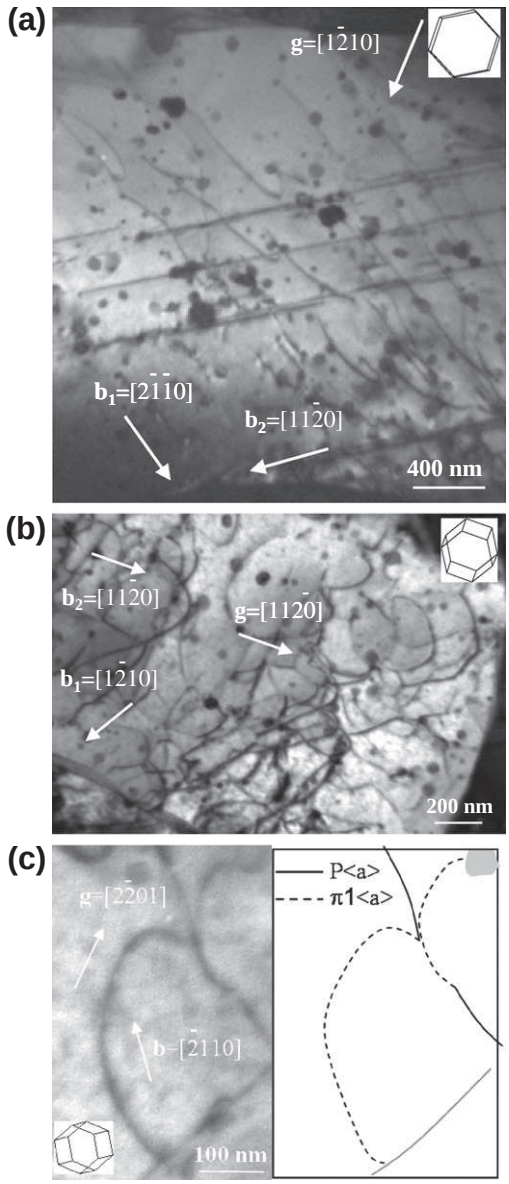

Fig. 6. Some features of dislocation glide. (a) Deformation of a grain by two prismatic slip systems ($g = [1\,-2\,1\,0]$, tilt $= -4°$), the main part of the dislocation lines observed present a quite screw character. (b) Deformation of a grain by two prismatic slip systems and mixed dislocation lines with a large curvatures ($g = [1\,1\,-2\,0]$, tilt $= -18°$). (c) Cross-slip occurrence in first pyramidal plane $\pi 1$ ($g = [2\,-2\,0\,1]$, tilt $= 26°$).

we can conclude that no evidence of dislocation climb is observed. However, this mechanism has been mentioned in recent studies of the mechanical behavior of Zr alloys investigating mechanical tests results [4,31] or mesoscopic observations [32]. That is why we will see in Section 5 if the hypothesis of dislocation climb can explain our experimental results in terms of geometrical considerations.

Dislocation configurations were analyzed to be mainly with an $\langle a \rangle$ Burgers vector, and inside prismatic or first order pyramidal planes (Fig. 6). $\langle c+a \rangle$ Burgers vectors, and basal or second order pyramidal planes concern less than 2% of the analyzed dislocation lines. Moreover, in accordance with previous studies [10,22], the $\pi_1\langle a \rangle$ glide takes place mostly through a cross-slip process. This is confirmed in our results by the fact that active $\pi_1\langle a \rangle$ glide exhibits a common $\langle a \rangle$ axis with $P\langle a \rangle$ glide in 96% of analyzed grains.

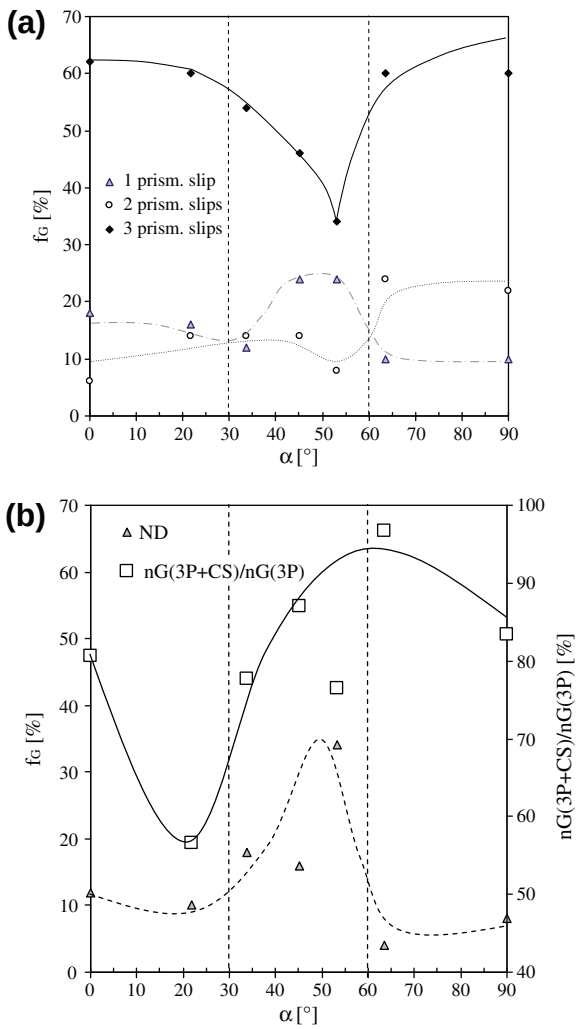

Fig. 7. (a) Variation of the number of activated prismatic slip systems P inside the observed grains (shown as a grain fraction f_G) vs. the loading direction α and the variation of associated Schmid factors. (b) Variation of the amount of grains exhibiting no plastic deformation (ND), or three activated prismatic slip systems with cross-slip (CS), or three activated prismatic slip systems.

The ability of a plastically deformed grain to contain one, two or three activated prismatic slip systems seems to depend on the loading direction (Fig. 7a). The occurrence of three prismatic slip systems in the same grain seems to be the main feature for all the loading orientations (the fraction of grains with 1 or 2 prismatic slips stays lower than 25%). Thus, the proportion of observed grains (written as a grain fraction f_G) carrying activated $P\langle a \rangle$ slip systems is quite constant in domain A, decreases in domain B and increases in domain C. We can see that this evolution is quite similar to the variation of Schmid factors vs. α. Consequently, a geometric approach of slip system activity seems to be suitable to describe plasticity in relation to crystallographic texture. Further, f_G varies oppositely to the amount of prismatic slip if the measured parameter considered is the proportion of grains carrying no plastic deformation (ND in Fig. 7b). On the other hand, the variation of cross-slip activation (CS) exhibits a hump in the "overstrengthening" behavior interval (domain B). This is illustrated in Fig. 7b by the variation of the ratio of grain population containing three cross-slipping prismatic slip systems divided by the grain population containing three prismatic slip systems: $n_G(3P + CS)/n_G(3P)$. Thus, we can consider that the cross-slip probability is higher in the B angular range than for the others (A and C). Additionally, the fraction of grains showing cross-slip activity decreases as a function of α in domains A and C. The correlation of these variations with those reported for the apparent activation volume V_{app} and the ratio of Schmid factors $F_S(\pi_1\langle a \rangle)/F_s(P\langle a \rangle)$ (Fig. 4) suggests two points:

– First, the frequency of activity of prismatic slip and pyramidal slip depends on the loading direction (α).
– Second, the anisotropy of sensitivity of the strain rate to macroscopic stress (expressed in term of V_{app}) observed as a function of loading direction (α) is mainly the consequence of a difference between the activation volume associated with prismatic and pyramidal slip.

4.3. Dislocation densities

For the seven specimens investigated, computations of dislocation densities in each observed grain enabled a plot of dislocation density distribution to be made. The results were then normalized and fitted by seven gamma functions. This method allows an accurate representation of experimental measurements, which can be interrelated with an analytical approach [33]. The seven variances of these functions were taken as root mean squares (RMSs) for dislocation densities distributions. The range of dislocation densities obtained here is not very wide. This can be explained by the absence of dislocation substructures or dislocation cells. Nevertheless, we can see that the loading direction seems to have similar effects on the RMS and the average dislocation density $\langle \rho \rangle$ (Fig. 8). Indeed, we observe an increase of both parameters in the "hard behavior" interval ($34° < \alpha < 53°$).

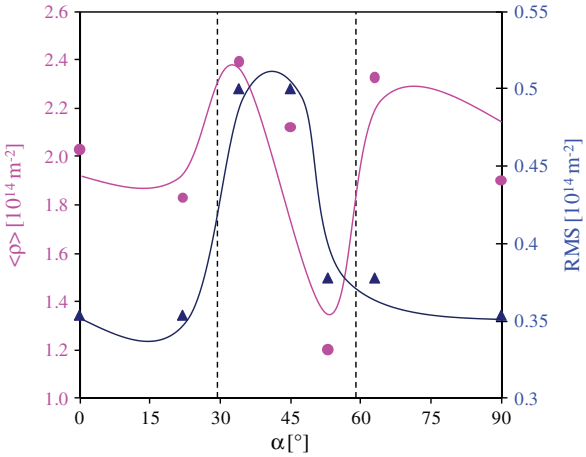

Fig. 8. Average dislocation density and RMS measured in the plastically deformed grains vs. the loading direction.

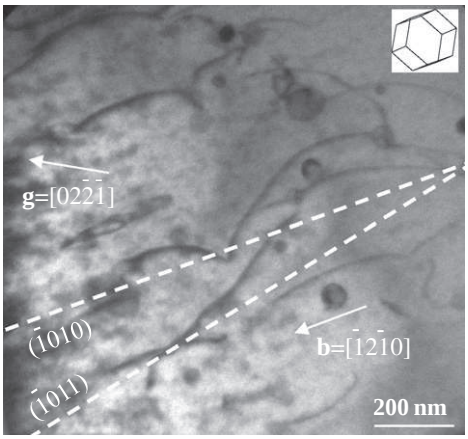

Fig. 9. Dislocations (screw in character) bowed in the pyramidal plane ($g = [02-2-1]$, tilt $= -7°$).

4.4. Long-range internal stresses

According to TEM observations, 90% of plastically deformed grains contain curved dislocations, localized on one slip system or more (Fig. 9). Radii of curvature of dislocation lines were measured in the appropriate slip plane. This provided an estimation of the amount of residual internal stresses inside the observed grains. It is possible that preparation of thin foils affects the repartition of these curvatures. Nevertheless, previous investigations (see Section 2.1) have shown that this process does not induce plastic deformation of grains. We therefore assume that the curvatures of dislocation lines observed on each sample all originate from the thermomechanical loading of the sample (heating, creep and cooling). Thus, if the frictional forces and the mobility of the pinning points are ignored, the radius of curvature R of a dislocation line can be linked to the line tension, corresponding to the absolute value of a local internal stress [34] $|\tau_i|$:

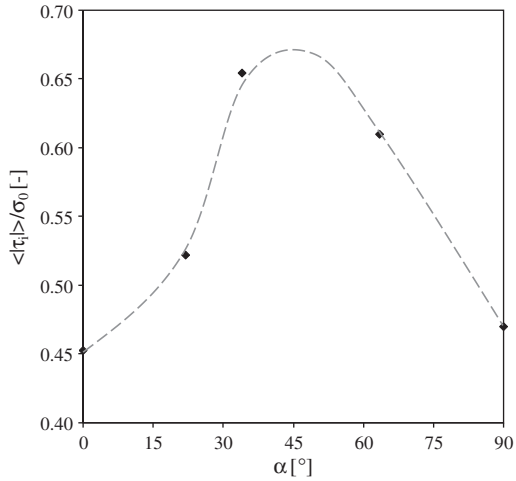

Fig. 10. Average internal stress measured in the plastically deformed grains vs. the loading direction.

$$\tau_i = \frac{\mu b}{4\pi(1-v)R} \ln\left(\frac{4R}{b} - 1\right) \tag{6}$$

where μ is the local shear modulus and v the Poisson ratio. The local internal stress can be either positive or negative, and its average value in the whole material equals zero as TEM observations are done without any mechanical loading. However, our method does not allow a determination of the sign of τ_i. Thus, computing the average values of $|\tau_i|$, written $\langle|\tau_i|\rangle$, we get an overview of the variation range of internal stresses inside the observed specimen, for a given loading direction. The higher the value of $\langle|\tau_i|\rangle$, the larger is this range, which is related to intergranular strain incompatibilities.

A part of $|\tau_i|$ is due to thermal dilatations incompatibilities, as crept samples are cooled from 673 K to room temperature before TEM observations. The internal stress induced by this process is possibly significant but independent of the loading direction α. Thus, only a comparative study of $|\tau_i|$ vs. α is allowed in our approach.

The values of $\langle|\tau_i|\rangle/\sigma_0$, calculated for the observed specimens, are presented in Fig. 10. We can see from this plot that this parameter reaches its highest values when α is between 30° and 60°. This result can be interpreted as an increase of intergranular plastic strain incompatibilities in domain B, resulting from the coexistence of two kinds of viscoplastic behaviors within the polycrystal.

As the present work investigates low strain conditions, only homogeneous intragranular dislocation distributions were observed. This suggests that significant evolutions of intragranular internal stresses cannot be obtained [34,35]. Thus, our results lead us to assume that the long-range internal stresses characterized in our crept samples originate from the intergranular phenomena.

5. Discussion

As explained in Section 1, creep anisotropy of the M5® alloy can be explained with physical and geometrical

considerations. The present results allow a discussion of assessments, leading to a multiscale characterization of this phenomenon. The first assumption that can be made is that creep anisotropy results from a transition between two microscopic deformation modes, involving both $P\langle a\rangle$ and $\pi_1\langle a\rangle$ slip systems. Both deformation modes correspond to the "oversoftening behavior" defined above (Fig. 3), i.e. in the neighborhood of purely axial or hoop loadings. The macroscopic evidence for the existence of those domains consists in different values of apparent activation volumes presented in Fig. 4. These activation volumes are probably linked to dislocation displacement mechanisms. Indeed, as frequent cross-slip and no dislocation structures were observed, dislocation production and annihilation should be easily activated [36].

Near axial loadings (domain A, $\alpha < 30°$), dislocation glide inside prismatic planes would control plastic deformation of the grain. For hoop loadings (domain C, $\alpha > 60°$), cross-slip activation would become a key parameter, which could explain the higher activation volume in this case. We can explain this hypothesis because a change from axial to hoop creep has a lower incidence on $\pi_1\langle a\rangle$ average Schmid factor than on $P\langle a\rangle$ average Schmid factor (Fig. 5). Thus, dislocation glide on these two slip systems seems to be a major contribution to creep anisotropy. This result is compatible with dislocation glide observed by several authors [2,10,13,37,38]. However, the possible intervention of dislocation climb mechanisms cannot be fully rejected yet. Indeed, jog dragging mechanisms can be enhanced by dislocation climb in crept zirconium alloys [5,39]. On the other hand, Viguier et al. calculated that jog displacements have a higher probability to occur along Burgers vectors [40]. Thus, displacement modes of observed dislocation jogs (Fig. 9) would certainly be better understood after in situ TEM experiments [37,41] on the studied alloy.

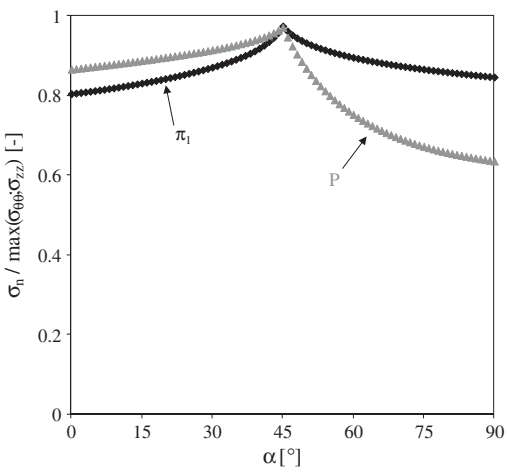

Fig. 11. Evolution with the loading direction of the ratio between normal (on best oriented prismatic (P) or first order pyramidal (π_1) planes) and applied stresses.

This experimental approach could also be useful to investigate generalized dislocation climb, as several studies [4,31,32] mention that this mechanism could control dislocation mobility [4]. Although dislocation climb was not observed in the present study, there is still a probability for it to be masked by dislocation rearrangement during the cooling of crept samples. However, Zr anisotropic self-diffusion [42] does not seem to be appropriate to explain creep anisotropy. And calculations, on the crystallographic texture of this study, of normal stresses on prismatic or first order pyramidal planes (Fig. 11) are not consistent with the overstrengthening observed during our creep tests in domain B. Furthermore, similar mechanical anisotropies have been observed in zirconium alloys at lower temperatures (298 K, 623 K) [10,11] where self-diffusion activation is negligible. This supports the assumption of two deformation modes involving dislocation glide mechanisms proposed in the present paper. Nevertheless, considering that evidences of dislocation climb at higher temperature have been presented in recent studies with macro- or mesoscopic considerations [4,31,32], we do not think that our conclusions apply above 450 °C.

The transition between both deformation modes occurs for domain B ($30° < \alpha < 60°$) and is associated with an apparent activation volume jump. As the main deformation mode differs here from one grain to another, long-range internal stresses increase (Fig. 10) inside plastically deformed grains. This enhances dislocation production, and therefore slightly higher dislocation densities (Fig. 8). The strong intergranular incompatibility in this case is confirmed by higher values of dislocation densities' RMS (Fig. 8) and TEM observations of a large number of grains carrying no plastic deformation (Fig. 7). The macroscopic consequence of these phenomena is the "overstrengthening behavior" defined above (Fig. 3). The globally heterogeneous response of the polycrystal for $30° < \alpha < 60°$ (domain B) can be linked to the difference of Schmid factor ratios for these loading directions (Figs. 4 and 5). Thus, the mechanical and geometrical approach proposed with the Schmid factors investigation is able to explain the creep anisotropy in the entire $0° < \alpha < 90°$ interval. Schmid factors being easily calculated by polycrystalline models [30,38,43,44], we can then assume that such models, applied to $P\langle a\rangle$ and $\pi_1\langle a\rangle$ dislocation glide, could accurately simulate multiaxial creep tests.

However, dislocation glide itself is not fully understood yet. Thus, the present results may enable the control of local deformation by any of these thermally activated mechanisms: cross-slip activation, frictional forces, interaction with solute or secondary phase obstacles [41,45]. In situ TEM investigation may be an appropriate experimental way to reduce this list (work in progress). In parallel, the present study should be extended to other temperatures in order to obtain activation energies. Such investigations would improve the accuracy of physically based models and enable their extension to other temperatures.

6. Conclusion

Although they are not sufficient to prove that climb mechanisms do not occur in Zr alloys, the present results contribute to show that dislocation glide could be the main physical parameter explaining creep anisotropy of M5® at 673 K. Its localization on $P\langle a\rangle$ and $\pi_1\langle a\rangle$ slip systems varies with the loading direction, according to statistical TEM measurements and geometric analyses associated with EBSD maps. We saw that these microscopic scale results, obtained on 50 grains per observed specimen, are in good accordance with mesoscopic and macroscopic analyses (EBSD and mechanical data). We therefore suggest that the physical basis of numerical modeling of recrystallized Zr alloys thermal creep should focus on dislocation glide on $P\langle a\rangle$ and $\pi_1\langle a\rangle$ slip systems, taking into account crystallographic texture considerations. This would logically lead to anisotropic creep behavior, especially in the case of tubes manufactured by the cold-pilgering process, as was recently illustrated [38].

To improve the understanding of thermal creep of recrystallized Zr alloys, the multiscale approach used in this study could be extended to other materials, other temperatures and be completed by in situ TEM experiments (work in progress). It would lead to the identification of the thermally activated mechanisms which control dislocation glide.

Acknowledgments

The authors would like to acknowledge here K. Niang (AREVA NP – CEZUS) and C. Grosjean for their contribution to the mechanical testing. TEM and EBSD facilities were provided with the help of E. Conforto (CCA – FREDD – Université de La Rochelle). Collaborations of Ph. Pilvin and A. Castro-Moreno (LIMATB – Université Bretagne Sud) were also greatly appreciated.

References

[1] Charit I, Murty KL. J Nucl Mater 2008;374(354):363.
[2] Brenner R, Béchade JL, Castelnau O, Bacroix B. J Nucl Mater 2002;305:175–86.
[3] Charquet D, Senevat J, Marcon JP. J Nucl Mater 1998;255:78–82.
[4] Hayes TA, Kassner ME, Rosen RS. Met Mater Trans A 2002;33A:337–43.
[5] Moon JH, Cantonwine JE, Anderson KR, Karthikeyan S, Mills MJ. J Nucl Mater 2006;353:177–89.
[6] Murty KL, Charit I. Prog Nucl Energy 2005;48:325–59.
[7] Murty KL. Mater Sci Eng 1985;70:169–80.
[8] Brachet JC, Béchade JL, Castaing A, Le Blanc L, Jouen T. Mater Sci Forum 1998;529:273–5.
[9] Tenckhoff E. In: ASTM-STP 966. Philadelphia (PA): ASTM; 1988.
[10] Geyer P. PhD Thesis, Ecole des Mines, Paris, France; 1999.
[11] Delobelle P, Robinet P, Geyer P, Bouffioux P. J Nucl Mater 1996;238:135–62.
[12] Domain C. In: Viguier B, editor. Plastox 2007. Paris: EDP Sciences; 2009.
[13] Ferrer F. PhD Thesis, Ecole Polytechnique, Palaiseau, France; 2000.
[14] Mardon JP, Garner GL, Hoffmann PB. In: Proceedings of the 2010 LWR fuel performance meeting, Orlando; 2010.
[15] Grosjean C, Poquillon D, Salabura JC, Cloué JM. Mater Sci Eng A 2009;510–511:332–6.
[16] Boudais C, Monceau D. CaRIne Crystallography V3.1© 1989–1998.
[17] Neuhaus R, Buchhagen P, Schwink C. Scripta Metall 1989;23:779–84.
[18] Feaugas X. Acta Mater 1999;47:3617–32.
[19] Feaugas X, Cavel M. Acta Metall 1997;45:2685–701.
[20] Feaugas X. Acta Mater 1997;45:2703–14.
[21] Helbert AL, Feaugas X. Scripta Mater 1997;36:1067–73.
[22] Geyer P, Feaugas X, Pilvin P. In: Plasticity'99, Cancun; 1999.
[23] Gentet D, Feaugas X, Risbet M, Lejeail Y, Pilvin P. Mater Sci Eng A 2010. http://dx.doi.org/10.1016/j.msea.2011.06.048.
[24] Feaugas X, Haddou H. Philos Mag 2007;87:989–1018.
[25] TSL Data Collection, 2005 TSL® OIM data collection for Windows; 2005.
[26] TSL-OIM Analysis, 2005 TSL® OIM Analysis for Windows; 2005.
[27] Bridier F, Villechaise P, Mendez J. Acta Mater 2005;53:555–67.
[28] Kocks UF. Met Trans 1970;1:1121–43.
[29] Feaugas X, Conforto E. In: Viguier B, editor. Plastox 2007. Paris: EDP Sciences; 2009.
[30] Priser M. PhD Thesis, Université Bretagne Sud, Lorient, France; 2011.
[31] Hayes TA, Rosen RS, Kassner ME. J Nucl Mater 2006;353:109–18.
[32] Perez-Prado MT, Barrabes SR, Kassner ME, Evangelista E. Acta Mater 2005;53:581–91.
[33] Risbet M, Feaugas X. Eng Fract Mech 2008;75:3511–9.
[34] Mughrabi H. Mater Sci Eng A 2001;309–310:237–45.
[35] Mughrabi H. Acta Mater 2006;54:3417–27.
[36] Jackson PJ. In: Proceedings of the conference to celebrate the fiftieth anniversary of the concept of dislocation in crystals, 11–12 December 1984. London: Institute of Metals; 1985.
[37] Couret A, Caillard D. Philos Mag A 1989;59:783–9.
[38] Priser M, Rautenberg M, Cloué JM, Pilvin P, Feaugas X, Poquillon D. J ASTM Int 2011;8:10–29.
[39] Soo P, Higgins GT. Acta Metall 1968;16:177–86.
[40] Viguier B, Hemker KJ, Bonneville J, Louchet F, Martin JL. Philos Mag A 1995;71:1295–312.
[41] Caillard D, Martin JL. Thermally activated mechanisms in crystal plasticity. Oxford: Pergamon; 2003.
[42] Christien F, Barbu A. J Nucl Mater 2005;246:272–81.
[43] Li W, Holt RA, Tracy S. J ASTM Int 2011;8.
[44] Lebensohn RA, Tomé CN. Acta Metall Mater 1993;41:2611–24.
[45] Derep JL, Ibrahim S, Rouby R, Fantozzi G. Acta Metall 1980;28:607–19.